Tunable spin and charge transport in silicene nanoribbons

Kh. Shakouri,[1,2,*] H. Simchi,[2] M. Esmaeilzadeh,[2] H. Mazidabadi,[2] and F. M. Peeters[1,†]
[1]*Departement Fysica, Universiteit Antwerpen, Groenenborgerlaan 171, B-2020 Antwerpen, Belgium*
[2]*Department of Physics, Iran University of Science and Technology, Narmak, Tehran 16844, Iran*
(Received 17 February 2015; published 10 July 2015)

Using the tight-binding formalism, we study spin and charge transport through a zigzag silicene ribbon subject to an external electric field E_z. The effect of an exchange field M_z is also taken into account and its consequences on the band structure as well as spin transport are evaluated. We show that the band structure lacks spin inversion symmetry in the presence of intrinsic spin-orbit interaction in combination of E_z and M_z fields. Our quantum transport calculations indicate that for certain energy ranges of the incoming electrons the silicene ribbon can act as a controllable high-efficiency spin polarizer. The polarization maxima occur simultaneously with the van Hove singularities of the local density of states. In this case, the combination of electric and exchange fields is the key to achieving nearly perfect spin polarization, which also leads to the appearance of additional narrow plateaus in the quantum conductance. Moreover, we demonstrate that the output current still remains completely spin-polarized for low-energy carriers even when a few edge vacancies are present.

DOI: 10.1103/PhysRevB.92.035413 PACS number(s): 73.63.−b, 73.22.−f, 85.75.−d

I. INTRODUCTION

Spintronics in ultrathin two-dimensional (2D) materials has recently attracted a lot of attention. In particular, graphene has recently been considered as a pioneering 2D crystal with very interesting spin and valley properties [1]. Graphene is a highly desirable material for coherent spin transport [2] because its spin-orbit interaction (SOI) is very weak [3,4]. However, it is known that the entanglement between spin and orbital degrees of freedom can be exploited to polarize the output current in a controllable way. This idea was first proposed for application in spin field-effect transistors [5,6]. Another 2D material that has a relatively strong SOI is graphene's silicon counterpart, called silicene. More recently, a field-effect silicene device has experimentally been realized by transferring silicene on a SiO_2/p^{++} substrate using a specific growth-transfer-fabrication process [7]. Moreover, silicene can be synthesized on Ag(111) and MoS_2 surfaces [8,9] and the stability of its free-standing-like version has been predicted by a number of theoretical studies [10]. The band structure of silicene is similar to that of graphene and the conduction and valence band edges are located at the corners of the Brillouin zone around the K and K' points. Contrary to graphene, silicene has a buckled structure and its intrinsic SOI opens a gap between the conduction and valence bands. Facilitated by this buckling, the band-gap edges of silicene are split by an external perpendicular electric field [11]. More interestingly, this splitting is of spin type—which is opposite for the two valleys—and can be tuned by varying the strength of the electric field [12].

Silicene's compatibility with silicon-based technology accompanied by the tunability of its structural band gap [12] further distinguishes it from other analogous 2D crystals such as MoS_2, which has a very strong spin-valley coupling. Thus far, these properties have stimulated extensive research such as the spin- and valley-polarized anomalous Hall effect [11,13], room-temperature field-effect transistor [7], giant magnetoresistance [14], and photo-induced topological phase transition [15], etc. Furthermore, recent studies proposed silicene as a potential candidate for application in spintronics and valleytronics devices [16–19].

In order to step beyond these works, here we investigate novel features of silicene and propose a versatile device whose working principle is based on an out-of-plane electric field. We consider a silicene ribbon with zigzag-terminated edges [see Fig. 1(a)]—in the presence of an exchange field—and show that this system can act as a high-efficiency spin polarizer. It is found that the application of a perpendicular electric field plays a key role not only for band-structure splitting but also in controlling the spin degree of freedom. Here we propose silicene ribbon as a field-effect spin device in which the process of manipulating spin is preformed electrically without any need to use external magnetic fields. We first address the effect of the electric and exchange fields on the band structure and show that the interplay of both fields induces spin asymmetry in the split energy subbands. Then, using the tight-binding Green's function (TBGF) formalism, we focus on ballistic spin and charge transport by evaluating the low-temperature quantum conductance. It is shown that a fully polarized spin current can be created by electrical gating of the silicene ribbon if an exchange field is simultaneously present. In this case, the maxima of spin polarization coincide with the van Hove singularities of the local density of states (LDOS). We also demonstrate that the induced spin polarization is highly resistant against the effect of a few edge vacancies.

The organization of the paper is as follows. In Sec. II, we give details of our model and formulate the strategies used to treat the problem of spin transport. The results of the calculations are summarized in Sec. III. We conclude with a summary in Sec. IV.

II. BASIC FORMALISM

A. Tight-binding description of silicene

The electronic properties of monolayer silicene near the K and K' points are described by a four-band tight-binding

*khosrow.shakouri@uantwerpen.be
†francois.peeters@uantwerpen.be

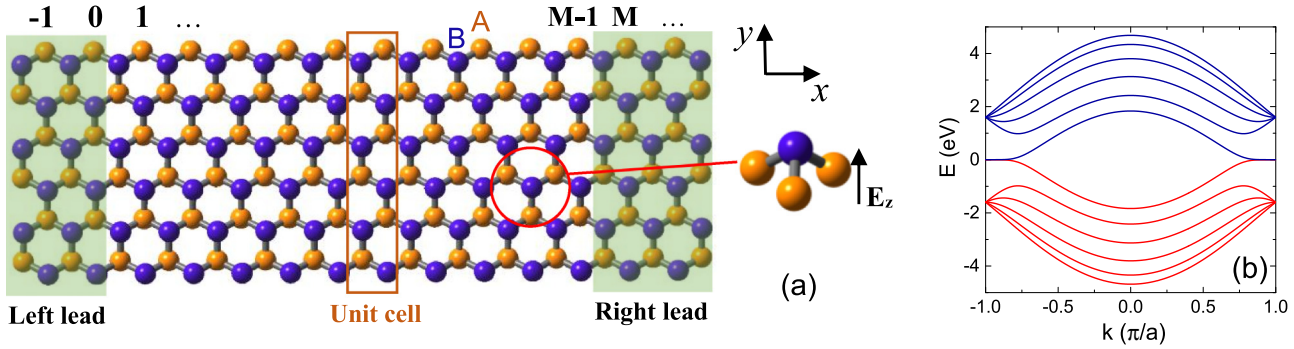

FIG. 1. (Color online) (a) The schematics of the transport channel consisting of a buckled silicene device connected to two semi-infinite silicene nanoribbons as the left and right leads. The system is similar to an iterative chain whose unit cell includes N silicon atoms. The silicene ribbon is subject to a perpendicular electric field E_z. (b) The band structure of an infinite silicene nanoribbon with zigzag-terminated edges for $N = 12$, and $E_z = M_z = 0$.

Hamiltonian that has previously been derived using first-principles calculations [11,17,20]. The symmetry arguments made in Ref. [20] show that the nearest-neighbor (NN) hopping terms do not contribute to the SOI, whereas the second-nearest-neighbor (SNN) ones create a SOI due to the buckled nature of the silicene structure. Such a buckling further separates vertically the A and B sublattices by a distance $2\ell = 0.46$ Å [11,16]. As a result, when a perpendicular electric field E_z is applied, a voltage difference of $2\ell E_z$ is created between the two sublattices, resulting in a staggered potential that an electron experiences while jumping between two NN sites. The strength of the first and second Rashba SOIs, arising from the NN and SNN hopping terms, respectively, are negligible compared to the intrinsic SOI λ_{so} and therefore we omit them in our calculations (the strength of the first and second Rashba SOIs are about 10 μeV and 0.7 meV, respectively [11]). In this case, taking only the intrinsic SOI into account, one can cast the Hamiltonian of silicene into a tight-binding expression,

$$H = -t\sum_{\langle i,j\rangle,\alpha} c^{\dagger}_{i\alpha}c_{j\alpha} + i\frac{\lambda_{so}}{3\sqrt{3}}\sum_{\langle\langle i,j\rangle\rangle,\alpha,\beta} v_{ij}c^{\dagger}_{i\alpha}(\sigma_z)_{\alpha\beta}c_{j\beta} + M_z\sum_{i,\alpha} c^{\dagger}_{i\alpha}\sigma_z c_{i\alpha} + e\ell E_z\sum_{i,\alpha}\xi_i c^{\dagger}_{i\alpha}c_{i\alpha} + \text{H.c.}, \quad (1)$$

where t is the hopping energy between the NN sites, $\langle i,j\rangle$ and $\langle\langle i,j\rangle\rangle$ denote the sum over NN and SNN hopping sites, respectively, α and β represent the spin quantum number, and the operator $c^{\dagger}_{i\alpha}$ ($c_{i\alpha}$) creates (annihilates) an electron with spin α at site i. The rest of the parameters in Eq. (1) are defined as follows: $\vec{\sigma}$ is the vector of Pauli's spin matrices, $v_{ij} = -1$ (+1) the clockwise (counterclockwise) hopping index with respect to the z axis, M_z is the exchange field and $\xi = \pm 1$ the valley index. Notice that the second term in Eq. (1) accounts for the intrinsic SOI due to the SNN contributions. The third term which involves the effect of an exchange field can be created on account of, e.g., the proximity with a ferromagnetic material [11,17,21]. The fourth term accounts for the effect of an electric field and critically distinguishes silicene from graphene.

By performing Fourier transformations and substituting the Pauli matrices σ_i, the discrete Hamiltonian (1) renders an effective Hamiltonian which is block diagonal in the spin degree of freedom. In the basis of $[|A\rangle, |B\rangle]^T \otimes [\uparrow,\downarrow]^T$, with T denoting the transpose, the explicit form of the effective Hamiltonian near the K valley is given by [22]

$$H = \begin{bmatrix} h^{+}(k) & 0 \\ 0 & h^{-}(k) \end{bmatrix}, \quad h^{\alpha}(k) = \begin{bmatrix} \alpha M_z + \Delta^{\alpha}_z & \hbar v_F k_- \\ \hbar v_F k_+ & \alpha M_z - \Delta^{\alpha}_z \end{bmatrix}, \quad (2)$$

where h^{+} (h^{-}) is for spin-up (spin-down), $k_{\pm} = k_x \pm ik_y$, $\Delta^{\alpha}_z = \alpha\lambda_{so} - e\ell E_z$ acts like a mass term in gapped graphene which determines the gap size between electron and hole energy surfaces, and v_F is the Fermi velocity. As is evident from Eq. (2), the band gap is closed for spin α upon canceling the intrinsic SOI term by applying an appropriate perpendicular electric field; i.e., Δ^{α}_z vanishes if $E_z = \alpha\lambda_{so}/e\ell$. For this reason and for the sake of inducing a large spin splitting we consider electric fields larger than this critical value.

Description of the transport channel. The setup of our system is illustrated in Fig. 1(a). The middle part consists of a zigzag silicene dot that is connected to two lateral homogeneous leads. The overall configuration of this system can be considered as a linear chain of iterative cells whose unit cell is an armchair strip of N silicon atoms [e.g., the structure shown in Fig. 1(a) has $N = 12$ atoms per unit cell]. The cells forming the left lead are located at sites $-\infty,\ldots,-1,0$ of the chain; likewise, those for the silicene dot are placed at $1,\ldots,M-1$ and for the right lead at $M, M+1,\ldots,\infty$. If the bulk periodicity parallel to these armchair cells is preserved, then the electron wave vector along the ribbon, k, is a good quantum number. This assumption provides a straightforward way to calculate the band structure within the tight-binding model. By applying Bloch's theorem, the k-dependent Hamiltonian can be written as

$$H_k = H_{00} + H_{01}e^{ika} + H_{-10}e^{-ika}. \quad (3)$$

Here, H_{00} is the Hamiltonian matrix for a unit cell at site 0 of the chain, H_{01} and H_{-10} describe the coupling with the right- and left-hand adjacent cells, respectively, and $a = 3.89$ Å is the lattice constant. The Hamiltonian (3) can readily be diagonalized in order to yield the energy dispersion as $H_k\psi_{nk} = E_{nk}\psi_{nk}$, where the Bloch state ψ_{nk} is a column vector in which the elements are a linear combination of

atomic orbitals at the lattice points. Furthermore, we obtain the site-resolved LDOS, along the width of the silicene ribbon, by evaluating $\rho_j(E) = \sum_{nk} |\psi^j_{nk}|^2 \delta(E - E_{nk})$, where $n = 1,2,\ldots,N$ is the subband index and j labels the atoms inside the unit cell.

B. Preliminaries for TBGF

Owing to the fact that the number of discrete sites goes to infinity in semi-infinite ribbons, we adopt an iterative algorithm [23–26] for the transport problem that allows for a very fast convergence. This technique was first introduced by Sancho *et al.* [23] to calculate transfer matrices and spectral density of states at the surface of semi-infinite crystals with stacked layers. A similar approach is simply applicable to an array of iterative cells building, e.g., the structure shown in Fig. 1(a) [24]. By implementing the algorithm one can easily determine the surface retarded Green's functions of the left and right leads which we denote by g^L_{00} and g^R_{MM}, respectively. Assuming that the isolated left and right leads are alike, which consequently confirms $H_{MM} = H_{00}$ and $H_{MM+1} = H_{-10}$, the surface Green's functions, using the transfer matrix approach, take the form [24,26]

$$g^L_{00}(E) = [(E + i\eta)\mathbf{I} - H_{00} - H^\dagger_{-10}\widetilde{T}]^{-1}, \tag{4}$$

and

$$g^R_{MM}(E) = [(E + i\eta)\mathbf{I} - H_{00} - H_{-10}T]^{-1}, \tag{5}$$

where $\mathbf{I}$ is the identity matrix, and the infinitesimal imaginary $i\eta$ moves the poles of the Green's function off the real axis and results in a retarded response. In Eqs. (4) and (5), the transfer matrices T and $\widetilde{T}$ can be calculated with the help of the expansions

$$T = t_0 + \widetilde{t}_0 t_1 + \widetilde{t}_0\widetilde{t}_1 t_2 + \cdots + \widetilde{t}_0\widetilde{t}_1\widetilde{t}_2\cdots t_\ell, \tag{6}$$

$$\widetilde{T} = \widetilde{t}_0 + t_0\widetilde{t}_1 + t_0 t_1\widetilde{t}_2 + \cdots + t_0 t_1 t_2\cdots\widetilde{t}_\ell, \tag{7}$$

where t_0 and $\widetilde{t}_0$ are defined as

$$t_0 = [(E + i\eta)\mathbf{I} - H_{00}]^{-1} H^\dagger_{-10}, \tag{8}$$

$$\widetilde{t}_0 = [(E + i\eta)\mathbf{I} - H_{00}]^{-1} H_{-10}, \tag{9}$$

and t_i and $\widetilde{t}_i$ obey the following recursion relations

$$t_i = (\mathbf{I} - \widetilde{t}_{i-1}t_{i-1} - t_{i-1}\widetilde{t}_{i-1})^{-1} t^2_{i-1}, \tag{10}$$

$$\widetilde{t}_i = (\mathbf{I} - \widetilde{t}_{i-1}t_{i-1} - t_{i-1}\widetilde{t}_{i-1})^{-1} \widetilde{t}^2_{i-1}. \tag{11}$$

The additive terms in Eqs. (6) and (7) have to be taken into account as long as t_ℓ and $\widetilde{t}_\ell$ tend to zero with arbitrary precision. As discussed in Ref. [23], with the help of this technique, a large set of 2^ℓ unit cells are incorporated in the calculations after ℓ iterations. The main advantage of this approach is that the number of iterations does not need an exponential increase, in particular, close to singularities of the Green's function.

Now, the next step is to calculate the surface Green's function inside the transport channel; i.e., inside the distinguished region from the lateral leads. To this end, we merge the sample with the right lead and return, layer by layer, back to obtain g^R_{22} by using the following recursion formula [26]:

$$g^R_{mm} = \left[(E + i\eta)\mathbf{I} - H_{mm} - H_{mm+1} g^R_{m+1m+1} H^\dagger_{mm+1}\right]^{-1}. \tag{12}$$

Finally, we can obtain the total Green's function g_{11} by taking into account the probability of scattering into the leads via the concept of self-energy [27,28]

$$g_{11} = [(E + i\eta)\mathbf{I} - H_{11} - \Sigma_L - \Sigma_R]^{-1}, \tag{13}$$

where

$$\Sigma_L = H^\dagger_{01} g^L_{00} H_{01}, \tag{14}$$

$$\Sigma_R = H_{12} g^R_{22} H^\dagger_{12}. \tag{15}$$

Furthermore, the broadening matrices including the coupling between transport channel with source and drain leads can be written as

$$\Gamma_{L(R)} = i(\Sigma_{L(R)} - \Sigma^\dagger_{L(R)}). \tag{16}$$

The important point to note is that the presence of an external electric field E_z, and/or of exchange term M_z, gives rise to a block-diagonal Green's function with spin-up and spin-down states:

$$g_{11} = \begin{bmatrix} g^\uparrow_{11} & 0 \\ 0 & g^\downarrow_{11} \end{bmatrix}. \tag{17}$$

Therefore, the transmission probability is given by

$$T^\alpha(E) = \mathrm{Tr}\left[\Gamma^\alpha_L g^\alpha_{11} \Gamma^\alpha_R (g^\alpha_{11})^\dagger\right], \quad \alpha = \uparrow,\downarrow. \tag{18}$$

Eventually, using the Landauer formula, the spin-resolved conductance through the silicene ribbon can be calculated as follows:

$$G^\alpha(E) = \frac{e^2}{h} T^\alpha(E). \tag{19}$$

The main advantage of the above notation is that one can easily calculate the spin polarization of the output current as follows:

$$p_s = \frac{G^\uparrow - G^\downarrow}{\sum_{\alpha=\uparrow,\downarrow} G^\alpha}. \tag{20}$$

For $0 < p_s \leqslant 1$ the dominant spin polarization corresponds to the spin-up state while for $-1 \leqslant p_s < 0$ the spin direction is reversed.

III. NUMERICAL RESULTS

We now address our main results obtained by assessing Eqs. (1) and (3), and also by implementing the TBGF method as detailed above. Subsequently, it will be shown that a zigzag silicene ribbon can act as a field-effect device that is tunable for both spin and charge transport. In order to elucidate the influence of an external electric field, and/or of exchange field, we first turn E_z and M_z off and then contrast the results with those obtained in the presence of them.

Band structure for $E_z = M_z = 0$. In the absence of any perpendicular electric and exchange fields, a zigzag silicene ribbon has the same energy dispersion as its graphene counterpart. This similarity has been illustrated in Fig. 1(b) for an infinite zigzag ribbon with width of $N = 12$ atoms.

TABLE I. Material parameters used in the calculations (see Ref. [20]).

	Quantity (unit)			
	t (eV)	λ_{so} (meV)	a (Å)	v_F (10^5 m/s)
Magnitude	1.6	3.9	3.86	5.52

Other fixed parameters used in the calculations are given in Table I. At the extreme left and right points, $k = \pm\pi/a$, the lowest two bands intersect the energy axis $E = 0$ and close the middle wide band gap between electron ($E > 0$) and hole ($E < 0$) states. This means that the band structure exhibits a metallic dispersion near the two corners of the Brillouin zone at $k = \pm\pi/a$. Similar to graphene-based zigzag ribbons, the low-lying energy bands are almost flat near these points revealing that the group velocity $v_g = \hbar^{-1}\partial E/\partial k$ is vanishingly small and the associated charge density is localized on the zigzag edges; see Ref. [29] and also the inset in Fig. 2 for $ka = \pi$. Since the energy scale shown in Fig. 1(b) is in units of electronvolts, the term due to the intrinsic spin-orbit coupling λ_{so} has no perceptible consequences for the band structure. We therefore switch to group velocity v_g and compare the results of the case $\lambda_{so} = 0$ (graphenelike case) with those for $\lambda_{so} = 3.9$ meV. The results are depicted in Fig. 2. The group velocity without the intrinsic term λ_{so} vanishes at $k = \pm\pi/a$, whereas the presence of λ_{so} induces a finite group velocity even for those electrons residing on the edges of the ribbon. Nevertheless, the induced velocity is very small compared to v_F. Notice also that the intrinsic SOI does not affect the charge density distribution along the armchair unit cell, as shown in the inset of Fig. 2, which can be deduced by the fact that $\lambda_{so} \ll t$.

Results for a perpendicular field E_z. Now the terms distinguishing the Hamiltonian of the silicene ribbon from that of the graphene-based ones become important, in particular, for low energies. Consequently, we focus our main attention on low-lying states around the $k = \pm\pi/a$ points. The band energy dispersion of a silicene ribbon with zigzag-terminated edges, consisting of $N = 48$ atoms per unit cell, is depicted in Figs. 3(a)–3(c) for three different E_z setups as specified by the small insets. The typical strength of the electric field considered in Figs. 3(b) and 3(c), i.e., $E_z = 40$ mV/ℓ, is of the order of V/nm, which is experimentally attainable [30]. By gating the silicene ribbon, an insulating gap opens between the electron and hole bands provided that the strength E_z is large compared to $\lambda_{so}/e\ell$ (as discussed above and also demonstrated in Ref. [11], the band gap is closed for the critical value $E_z = \lambda_{so}/e\ell$ and converts the material into a spin-valley-polarized metallic system). In Fig. 3(c), it is evident that the application of an asymmetric perpendicular electric field $E_z \propto \Theta(y - w/2)$—here, Θ is the Heaviside step function and w the ribbon width—halves the energy gap asymmetrically. Moreover, as seen in Figs. 3(b) and 3(c), the electric field lifts the spin degeneracy of all electronic states so that the spin-split bands have spin inversion symmetry with respect to the boundary of the Brillouin zone at $k = \pi/a$. Based on this symmetry we conclude that $E_k^{\uparrow} = E_{-k}^{\downarrow}$ because any k wave vector larger than π/a can be translated into the first zone by the lattice vector $K_a = -2\pi/a$. However, we show next that the E_z-induced spin splitting does not suffice, on its own, to create a spin-polarized current. Figures 3(d)–3(f) show the charge conductance through the silicene ribbon, $G = (e^2/h)\sum_{\alpha=\uparrow,\downarrow} T^{\alpha}$, in terms of the chemical potential of the left lead, for the same electric fields as in Figs. 3(a)–3(c), respectively. On the right side, the chemical potential is assumed to be zero $\mu_R = 0$. The quantized conductance plateaus as well as the successive transitions with height $4e^2/h$ (the factor 4 is responsible for spin and sublattice pseudospin indexes) are clearly observable [26,31,32]. By applying an external electric field, the induced band gap between electron and hole states suppresses the transmission of low-energy carriers with $|\mu_L| < e\ell E_z$. Therefore, in Fig. 3(b), the width of the region depleted from conducting carriers is about $2e\ell E_z$. The remarkable feature of this kind of transport suppression is that the charge carriers respond to an out-of-plane electric field which creates an intrasublattice barrier between vertically separated A and B sublattices. The number of interplateau transitions appearing in G is locked to the width of the zigzag ribbon, i.e., the number of atoms that constitute a unit cell. The reason stems from the fact that an increase of N adds more subbands (transverse modes) into the band structure, whereas the spacing between furthest bands at $E \approx \pm 4.8$ eV [see Fig. 1(b)] remains unchanged. Indeed, the bottom of these subbands coincide with the peaks of the DOS as well as with the transition regions between two successive plateaus as is obvious in Fig. 4 (similar reasoning is presented in Ref. [32] for a graphene ribbon). It is noteworthy that this effect can also be interpreted on the basis of physical concepts describing the quantization of the conductance through point contacts [28,33]. Therefore, with the assumption that the transport regime of the point contact and leads is ballistic, the conductance directly depends on the number of channels that contribute to transport. The decline of G which is seen in Fig. 4 occurs due to inversion of the sign of the effective mass $m^* \propto \partial^2 E/\partial k^2$, where the electron-type bands are replaced

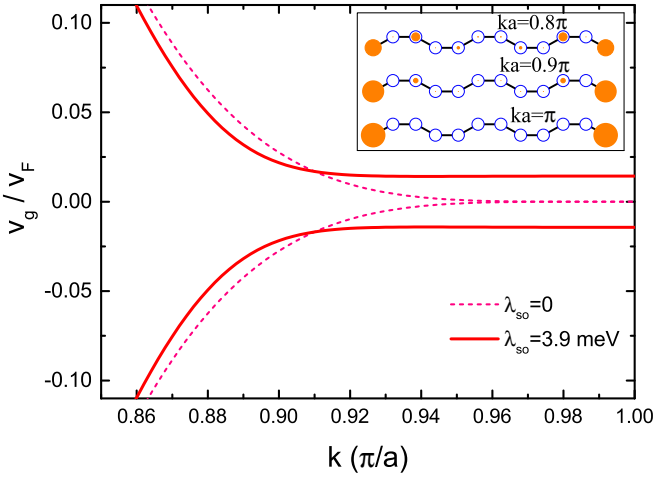

FIG. 2. (Color online) The group velocity of the edge states near $k = \pi/a$ for $\lambda_{so} = 0$ (dashed curve) and $\lambda_{so} = 3.9$ meV (solid curve). The inset shows the charge density distribution over an armchair unit cell, comprising of $N = 12$ atoms, for three different Bloch wave vectors k.

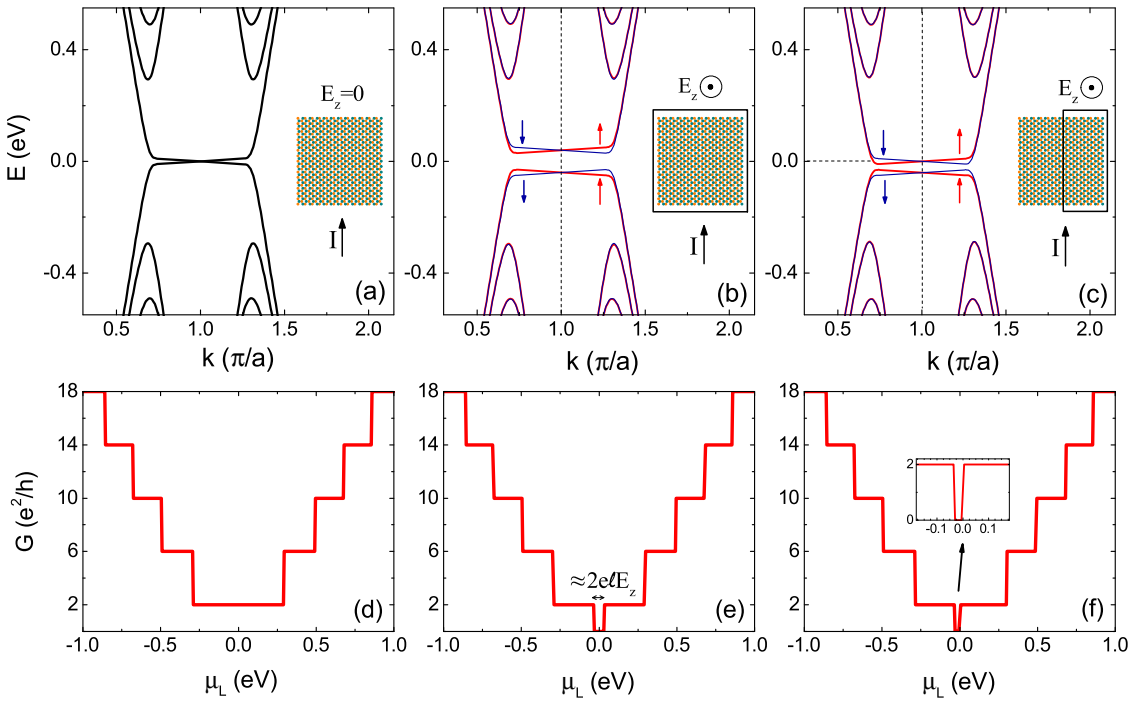

FIG. 3. (Color online) The band structure of a silicene nanoribbon with zigzag-terminated edges subject to the following perpendicular electric fields: (a) $E_z = 0$, (b) $E_z = 40\ \mathrm{mV}/\ell$, and (c) a steplike electric field with $E_z = 40\Theta(y - w/2)\ \mathrm{mV}/\ell$. The electric field $E_z \gg \lambda_{so}/e\ell$ opens a sizable gap between electron and hole states. Panels (d), (e), and (f) show the charge conductance of incoming electrons vs μ_L for the same electric fields as in (a), (b), and (c), respectively.

by hole-type ones. In this case, the conductance plateaus are accompanied by maxima of energy subbands. Using a similar analysis, one finds that the subbands with opposite spins, shown in Figs. 3(b) and 3(c), have equal contributions in spin transport. The reason can be attributed to the fact that the spin-split subbands are qualitatively alike and their minima occur at the same energy.

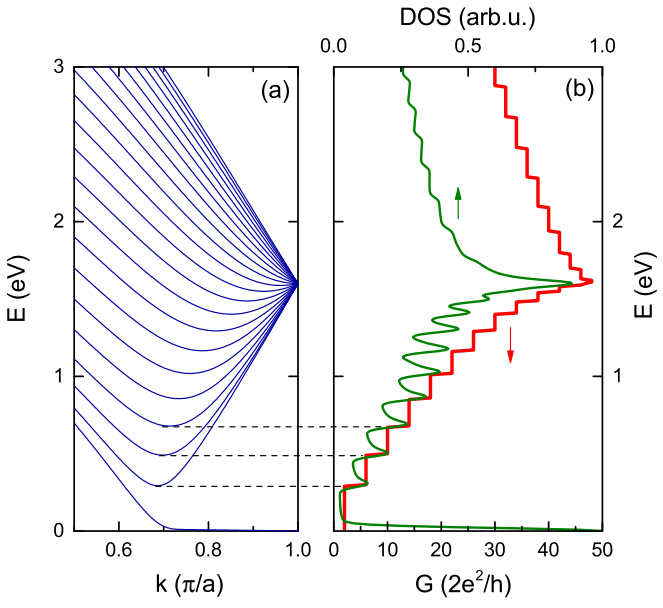

FIG. 4. (Color online) (a) The band structure of a zigzag silicene ribbon with $N = 48$ near the boundary of the Brillouin zone. (b) The quantum conductance G (the red curve referred to the bottom axis) and the density of states (the green curve referred to the top axis) as function of the energy. The subbands coincide with the transition regions between the plateaus of G.

Taking into account only the exchange field, the band structure is split again into opposite spin states. However, unlike the previous case, spin inversion occurs with a reflection in energy with respect to the $E = 0$ axis: An electron band with spin-up corresponds to a hole band with spin-down, i.e., $E^{\uparrow}(k) = -E^{\downarrow}(k)$, and vice versa; see the magnified area in Fig. 5(a). The lowest electron- (solid curves) and hole-type (dashed-dotted curves) subbands with positive and negative effective masses, respectively, have a common contact point at $k = \pi/a$. Therefore, each subband is expected to cancel the other's contribution in spin transport following the same analysis as given above. Although this problem does not affect the upper subbands, the mixing of spin-up and spin-down states prevents perfect spin polarization. To resolve this drawback we examine the presence of a uniform E_z field in addition to M_z. The result of this case is summarized in Fig. 5(b). As seen, the interplay between E_z and M_z fields creates an asymmetry in the band structure. Indeed, each of these fields splits the band structure in a certain way, which results in a spin asymmetry when both mechanisms of spin splitting are present.

In Fig. 6 we plot the spin-resolved conductance G^{α}, $\alpha = \uparrow, \downarrow$, as a function of the chemical potential of incoming electrons for $E_z = 40\ \mathrm{mV}/\ell$ and $M_z = 2\lambda_{so}$. The asymmetry of the band structure induces a sizable spin gap ($\Delta\mu_L \approx 18$ meV) in quantum conductance transitions and leads to the separation of opposite spin contributions in the conductance. Another consequence of the asymmetry of the band structure

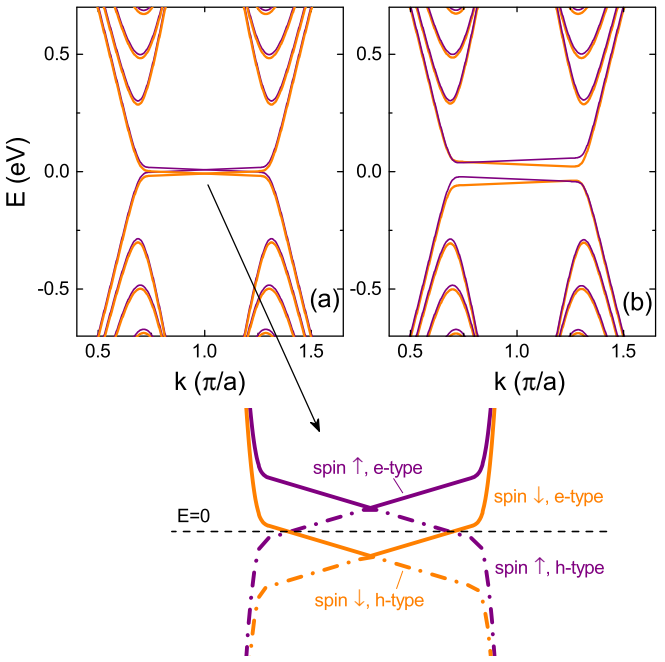

FIG. 5. (Color online) The band structure of a silicene ribbon with $N = 48$ for $E_z = 0$ (a) and $E_z = 40$ mV/ℓ (b), in the presence of an exchange field $M = 2\lambda_{so}$. The purple (orange) curves indicate energy dispersion of spin-up (spin-down) state. The enlarged area (bottom figure) reveals that the band structure has spin inversion symmetry with respect to the $E = 0$ axis.

is the appearance of narrow plateaus in the charge conductance (see the inset in Fig. 6), which originates from the superiority of one spin plateau over another. The width of the transition regions between spin-split plateaus is very small and disappears with increasing energy of mobile carriers. To better assess the

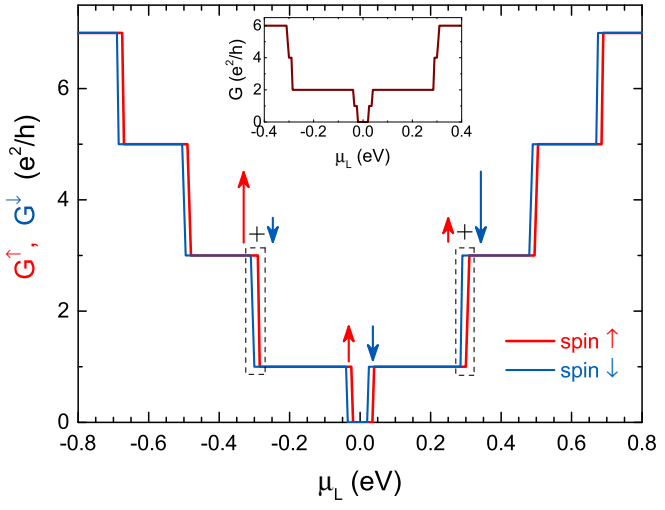

FIG. 6. (Color online) (a) Spin-resolved conductance, $G^{\uparrow}$ (red line) and $G^{\downarrow}$ (blue line), as a function of the chemical potential of the incoming electrons. The inset displays the overall (charge) conductance $G = G^{\uparrow} + G^{\downarrow}$. Additional narrow plateaus in the quantum conductance can be traced to the discrepancy of the contribution of opposite spins.

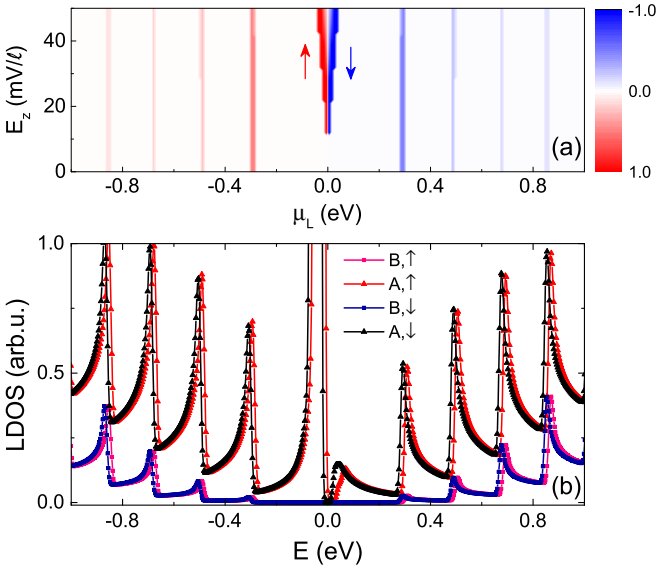

FIG. 7. (Color online) (a) Contour map of spin polarization p_s vs the energy of incoming carriers as well as applied electric field E_z. Each unit cell consists of $N = 48$ atoms. (b) The spin-resolved LDOS near the zigzag-terminated edges for the two atomic sites specified by the A and B sublattice indexes.

role of the combination of electric and exchange fields in spin transport, the contour plot of spin polarization p_s is shown as function of the electric field E_z and the chemical potential of the incoming electrons μ_L; see Fig. 7(a). The exchange field is assumed to be fixed as $M_z = 2\lambda_{so}$. As seen, a nearly perfect spin polarization is attainable for low-energy incoming carriers as long as $E_z \gtrsim 12$ mV/ℓ. Conversely, in the absence of the electric field, the output current does not exhibit any spin polarization when the value $|\mu_L|$ belongs to the energy range below 0.28 eV, which corresponds to the onset of the second energy subband. In addition, the spin direction of the polarized conductance is opposite for the electron- and hole-type charge carriers with $\mu_L > 0$ and $\mu_L < 0$, respectively.

Another important feature of the resonant lines in the map of spin polarization, shown in Fig. 7(a), is that they occur precisely accompanied by the sharp peaks (van Hove singularities) of the LDOS illustrated in Fig. 7(b). The van Hove singularities, which here reflect the onset of quasi-1D energy subbands, have been experimentally observed in similar 1D structures such as for ordered grain boundaries of graphene [34] or carbon nanotubes [35]. Notice that a similar result for the LDOS as in Fig. 7(b) can be obtained by calculating the imaginary part of the surface Green's function, i.e., $\rho_j(E) = -\frac{1}{\pi}\mathrm{Im}\, g_{mm}(j,j)$.

Effect of lattice vacancy at zigzag edges. A typical defect that usually influences the edges of 2D honeycomb structures is the existence of lattice vacancies [36,37]. We simulate a vacancy by setting the corresponding on-site energy to infinity [26,38], which impedes the occupation of the vacant site by mobile carriers. The charge conductance in the presence of a few vacant sites is depicted in Fig. 8(a) when an atom with sublattice index A, two atoms with unequal sublattice indexes, or three nearest atoms with A, B, and A sublattice indexes are unilaterally removed from one of the zigzag

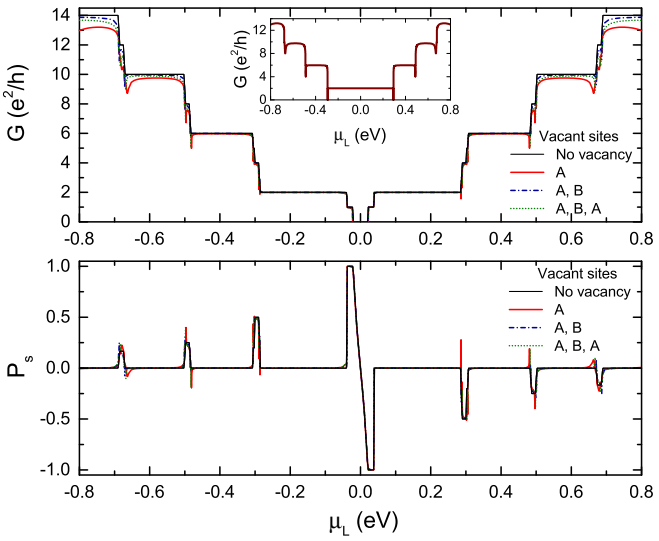

FIG. 8. (Color online) (a) The charge conductance of a zigzag ribbon with one (solid red line), two (dash-dotted blue line), and three (dotted green line) vacancies. The perpendicular electric field is $E_z = 40\ \mathrm{mV}/\ell$, $N = 48$, and the exchange field is assumed to be $M_z = 2\lambda_{so}$. The thin solid line shows the conductance of a perfect ribbon. The inset shows the charge conductance of a graphenelike system with $\lambda_{so} = E_z = M_z = 0$. (b) Spin polarization p_s as a function of the energy of incoming electrons.

edges. To better appreciate the effect of this kind of defect, the conductance curve of a perfect ribbon is also shown for reference by a thin solid line. From a detailed comparison one can find that the main difference between the cases with and without defect is almost limited to the transition regions connecting the discontinuous plateaus of the perfect ribbon. The early calculations [26] that have been performed for the LDOS demonstrate that the van Hove singularities are particularly altered around the vacant lattice sites [38]. Noting that these singular peaks coincide with the step transitions shown in Fig. 4(b) and Fig. 6, for that reason the main effect of such defect is observed in these regions. More importantly, a single vacancy in graphenelike systems without SOI and E_z- and M_z-dependent terms is expected to create quasilocalized stats with zero-conductance dips [26]—at the place of the first transition—which are illustrated in the inset of Fig. 8(a). However, for a silicene ribbon this is not the case for two reasons: The conductance transitions and thus the zero-conductance dip points are split due to the electric and exchange fields and that the intrinsic SOI results in a finite group velocity.

Although the edge vacancies affect slightly the step transitions of the charge conductance, there is still a fully polarized spin conductance with $p_s = \pm 1$ for the low-energy carriers, which is shown in Fig. 8(b). As seen, the oscillations of p_s first start with pronounced peaks but they gradually damp with increasing carrier energy. The reason can be traced to the fact that the difference between up and down spin conductances is always constant near the transition regions, i.e., $G^{\uparrow} - G^{\uparrow} = 2e^2/h$, while both $G^{\uparrow}$ and $G^{\downarrow}$ retain their step increase with energy. In addition, the spacing between spin-split bands decreases when M_z and $e\ell E_z$ are both very small compared to μ_L. Notice that spin polarization can be simply inverted by reversing the electric field.

IV. SUMMARY

We have investigated spin and charge transport through a zigzag silicene nanoribbon in the presence of external electric and exchange fields. When only one of the aforementioned fields is present, the band structure of the silicene ribbon is split symmetrically into opposite spin states; the application of only an out-of-plane electric field leads to spin inversion with respect to the k axis, i.e., $E^{\uparrow}(k) = E^{\downarrow}(-k)$, whereas the presence of the exchange field creates spin inversion with respect to the energy axis, $E^{\uparrow}(k) = -E^{\downarrow}(k)$. Due to the opening of energy subbands, ballistic transport results in quantized conductance with steplike transitions. It was shown that both spin states contribute identically to spin transport when $M_z = 0$, $E_z \neq 0$, while a partially polarized spin current is attainable for the case of $M_z \neq 0$ and $E_z = 0$. To compensate for this drawback, in order to create a perfect spin polarization, we showed that the simultaneous inclusion of both E_z and M_z fields is required. In this case, it is found that the interplay between both fields induces a spin asymmetry in the band structure. Because of spin asymmetry, additional spin-resolved plateaus appear in the quantum conductance, which allows the realization of a high-efficiency spin polarizer. We also have assessed the effect of a few edge vacancies and showed that this type of defect has no perceptible consequences for the induced spin polarization.

[1] D. Pesin and A. H. MacDonald, Nat. Mater. **11**, 409 (2012).

[2] T. Maassen, J. J. van den Berg, N. IJbema, F. Fromm, T. Seyller, R. Yakimova, and B. J. van Wees, Nano Lett. **12**, 1498 (2012).

[3] J. C. Boettger and S. B. Trickey, Phys. Rev. B **75**, 121402(R) (2007).

[4] Y. Yao, F. Ye, X.-L. Qi, S.-C. Zhang, and Z. Fang, Phys. Rev. B **75**, 041401 (2007).

[5] S. Datta and B. Das, Appl. Phys. Lett. **56**, 665 (1990).

[6] S. A. Wolf, D. D. Awschalom, R. A. Buhrman, J. M. Daughton, S. von Molnár, M. L. Roukes, Y. Chtchelkanova, and D. M. Treger, Science **294**, 5546 (2001).

[7] L. Tao, E. Cinquanta, D. Chiappe, C. Grazianetti, M. Fanciulli, M. Dubey, A. Molle, and D. Akinwande, Nat. Nanotech. **10**, 227 (2015).

[8] P. Vogt, P. De Padova, C. Quaresima, J. Avila, E. Frantzeskakis, M. C. Asensio, A. Resta, B. Ealet, and G. Le Lay, Phys. Rev. Lett. **108**, 155501 (2012); A. Fleurence, R. Friedlein, T. Ozaki, H. Kawai, Y. Wang, and Y. Yamada-Takamura, *ibid.* **108**, 245501 (2012).

[9] D. Chiappe, E. Scalise, E. Cinquanta, C. Grazianetti, B. v. Broek, M. Fanciulli, M. Houssa, and A. Molle, Adv. Mater. **26**, 2096 (2014).

[10] Y. Cai, C.-P. Chuu, C. M. Wei, and M. Y. Chou, Phys. Rev. B **88**, 245408 (2013); H. Liu, J. Gao, and J. Zhao, J. Phys. Chem. C **117**, 10353 (2013); G. R. Berdiyorov, M. Neek-Amal, F. M. Peeters, and Adri C. T. van Duin, Phys. Rev. B **89**, 024107 (2014).
[11] M. Ezawa, Phys. Rev. Lett. **109**, 055502 (2012); New J. Phys. **14**, 033003 (2012).
[12] Z. Ni, Q. Liu, K. Tang, J. Zheng, J. Zhou, R. Qin, Z. Gao, D. Yu, and J. Lu, Nano Lett. **12**, 113 (2011).
[13] H. Pan, Z. Li, C.-C. Liu, G. Zhu, Z. Qiao, and Y. Yao, Phys. Rev. Lett. **112**, 106802 (2014).
[14] C. Xu, G. Luo, Q. Liu, J. Zheng, Z. Zhang, S. Nagase, Z. Gaoa, and J. Lu, Nanoscale **4**, 3111 (2012).
[15] M. Ezawa, Phys. Rev. Lett. **110**, 026603 (2013).
[16] C. J. Tabert and E. J. Nicol, Phys. Rev. Lett. **110**, 197402 (2013).
[17] W.-F. Tsai, C.-Y. Huang, T.-R. Chang, H. Lin, H.-T. Jeng, and A. Bansil, Nat. Commun. **4**, 1500 (2013).
[18] Kh. Shakouri, P. Vasilopoulos, V. Vargiamidis, G.-Q. Hai, and F. M. Peeters, Appl. Phys. Lett. **104**, 213109 (2014); Kh. Shakouri, P. Vasilopoulos, V. Vargiamidis, and F. M. Peeters, Phys. Rev. B **90**, 235423 (2014).
[19] X.-T. An, Y.-Y. Zhang, J.-J. Liu, and S.-S. Li, New J. Phys. **14**, 083039 (2012).
[20] C.-C. Liu, H. Jiang, and Y. Yao, Phys. Rev. B **84**, 195430 (2011).
[21] T. Yokoyama, Phys. Rev. B **87**, 241409(R) (2013).
[22] B. Van Duppen, P. Vasilopoulos, and F. M. Peeters, Phys. Rev. B **90**, 035142 (2014).
[23] M. P. Lopez Scancho, J. M. Lopez Sancho, and J. Rubio, J. Phys. F: Met. Phys. **14**, 1205 (1984).
[24] M. Buongiorno Nardelli, Phys. Rev. B **60**, 7828 (1999).
[25] M. Esmaeilzadeh and S. Ahmadi, J. Appl. Phys. **112**, 104319 (2012); H. Simchi, M. Esmaeilzadeh, and M. Heydarisaani, Phys. Status Solidi B **249**, 9 (2012).
[26] T. C. Li and S.-P. Lu, Phys. Rev. B **77**, 085408 (2008).
[27] M. Paulsson and M. Brandbyge, Phys. Rev. B **76**, 115117 (2007).
[28] Supriyo Datta, *Quantum transport: Atom to Transistor* (Cambridge UNiversity Press, Cambridge, U.K., 2005).
[29] K. Nakada, M. Fujita, G. Dresselhaus, and M. S. Dresselhaus, Phys. Rev. B **54**, 17954 (1996).
[30] J. B. Oostinga, H. B. Heersche, X. Liu, A. F. Morpurgo, and L. M. K. Vandersypen, Nat. Mater. **7**, 151 (2007); Y. Zhang, T.-T. Tang, C. Girit, Z. Hao, M. C. Martin, A. Zettl, M. F. Crommie, Y. R. Shen, and F. Wang, Nature (London) **459**, 820 (2009).
[31] H. Rostami and R. Asgari, Phys. Rev. B **88**, 035404 (2013).
[32] J. Baringhaus, M. Ruan, F. Edler, A. Tejeda, M. Sicot, A. Taleb-Ibrahimi, A.-P. Li, Z. Jiang, E. H. Conrad, C. Berger, C. Tegenkamp, and W. A. de Heer, Nature (London) **506**, 349 (2014).
[33] B. J. van Wees, H. van Houten, C. W. J. Beenakker, J. G. Williamson, L. P. Kouwenhoven, D. van der Marel, and C. T. Foxon, Phys. Rev. Lett. **60**, 848 (1988).
[34] C. Ma, H. Sun, Y. Zhao, B. Li, Q. Li, A. Zhao, X. Wang, Y. Luo, J. Yang, B. Wang, and J. G. Hou, Phys. Rev. Lett. **112**, 226802 (2014).
[35] J. W. G. Wildöer, L. C. Venema, A. G. Rinzler, R. E. Smalley, and C. Dekker, Nature (London) **391**, 59 (1998).
[36] Y. Kobayashi, K.-I. Fukui, T. Enoki, and K. Kusakabe, Phys. Rev. B **73**, 125415 (2006).
[37] Y. Niimi, T. Matsui, H. Kambara, K. Tagami, M. Tsukada, and H. Fukuyama, Phys. Rev. B **73**, 085421 (2006).
[38] L. Chico, L. X. Benedict, S. G. Louie, and M. L. Cohen, Phys. Rev. B **54**, 2600 (1996).